

**CLASSIFYING ORBITS OF LOW AND HIGH ENERGY STARS IN  
AXISYMMETRIC DISK GALAXIES**

Euaggelos E. Zotos

*Department of Physics, School of Science, Aristotle University of Thessaloniki,  
GR-541 24, Thessaloniki, Greece; e-mail: evzotos@physics.auth.gr*

Received: 2015 May 1; accepted: 2015 June 26

**Abstract.** The ordered or chaotic character of orbits of stars moving in the meridional  $(R, z)$  plane of an analytic axisymmetric time-independent disk galaxy model with an additional spherically symmetric central nucleus is investigated. Our aim is to determine how the total energy influences the orbital structure of the galaxy. For this purpose we monitor how the percentage of chaotic orbits as well as the rates of orbits composing the main regular families evolve as a function of the value of the energy. In order to distinguish with certainty between chaotic and ordered motion we use the SALI method in extensive sets of initial conditions of orbits. Moreover, a spectral method is applied for identifying the various regular families and also for recognizing the secondary resonances that bifurcate from them. Our numerical computations suggest that for low energy levels the observed amount of chaos is high and the orbital content is rather poor, while for high energy levels, corresponding to global motion, regular motion dominates and many secondary higher resonances emerge. We also compared our results with previous related work.

**Key words:** galaxies: kinematics and dynamics – galaxies: structure, chaos

**1. INTRODUCTION**

A first step towards understanding the overall orbital content of a galaxy model is to know whether the orbits of stars are ordered or chaotic. Another issue of significant importance is the distribution of ordered orbits into different families. For this particular purpose, more than thirty years ago, Binney & Spergel (1982, 1984) introduced a method based on spectral dynamics. This technique was improved and extended later on by Laskar (1993) and Carpintero & Aguilar (1998). The main advantage of this method is the calculation of the ratio of the integers which corresponds to the ratio of the main frequencies of the orbit, where main frequency is the frequency of the greatest amplitude in each coordinate. The computation of the frequencies is obtained by the frequency Fourier transform, a routine initially developed by Laskar (1988) and later substantially improved by Šidlichovský & Nesvorný (1996). In this work, we shall deploy this method in order to identify the resonant classification of regular orbits and categorize them

into different families.

Recently, in a series of papers (Caranicolas & Zotos 2013; Zotos & Caranicolas 2013; Zotos 2014a,b) we classified orbits in several types of galaxy models containing dark matter haloes. These papers act as a guide regarding the structure and the numerical methods of the present work. Furthermore, in other recent papers we performed orbit classification in new galaxy models (Zotos & Caranicolas 2014), or we investigated specific features of well-known galactic systems, such as the influence of the angular momentum (Zotos 2014c) and the mass transportation from the disk to the nucleus (Zotos 2014d).

In Zotos & Carpintero (2013) (hereafter Paper I) we introduced a composite analytic, axially symmetric galactic gravitational model that embraces the general features of a disk galaxy with a dense massive spherical nucleus. Then we distinguished between regular and chaotic motion of stars moving in the meridional  $(R, z)$  plane. We also performed an orbit classification by separating regular orbits into different families, thus revealing how some important quantities of the system affect the orbital structure. In the present paper we shall use the same galactic model in an attempt to determine the properties of low and high energy stars.

The paper is organized as follows: the properties of the galactic gravitational model are presented in Section 2, while all of the computational methods used for determining the character of orbits are described in Section 3. In the following section we examine how the total energy influences the orbital structure of the galaxy by measuring the corresponding percentages of all types of orbits. In Section 5 we conduct an overview analysis using a continuous spectrum of energy values. The article ends with Section 6, where the conclusions of our work are presented.

## 2. PROPERTIES OF THE GALACTIC MODEL

The aim of this numerical investigation is to classify the orbits of low and high energy stars moving in the meridional  $(R, z)$  plane of an axisymmetric disk galaxy with an additional spherically symmetric nucleus. In our calculations we use cylindrical coordinates  $(R, \phi, z)$ , where  $z$  is the axis of symmetry of the galaxy.

Let us briefly recall the galactic gravitational model which was introduced in Paper I. The total analytical gravitational potential  $\Phi(R, z)$  is time-independent and consists of two main components: the potential of the central nucleus,  $\Phi_n$ , and that of the flat disk,  $\Phi_d$ . In order to describe the properties of the nucleus we apply a spherically symmetric Plummer potential (see, e.g., Binney & Tremaine 2008)

$$\Phi_n(R, z) = -\frac{GM_n}{\sqrt{R^2 + z^2 + c_n^2}}, \quad (1)$$

where  $G$  is the gravitational constant, while  $M_n$  and  $c_n$  are the mass and the scale length of the nucleus, respectively. It should be pointed out that similar types of potentials have been successfully used in previous works to model the properties of central mass concentrations in galaxies (see, e.g., Hasan & Norman 1990; Hasan et al. 1993; Zotos 2012; Zotos & Carpintero 2013; Zotos 2014a). Moreover, we would like to emphasize that the central nucleus represents a bulge rather than a black hole or any other compact stellar object and therefore we do not take into account any relativistic effects.

To represent the flat galactic disk we use the potential of the Miyamoto & Nagai

(1975) form:

$$\Phi_d(R, z) = -\frac{GM_d}{\sqrt{R^2 + (\alpha + \sqrt{h^2 + z^2})^2}}. \quad (2)$$

Here  $M_d$  is the mass of the disk,  $\alpha$  is the horizontal scale length of the disk and  $h$  corresponds to the vertical scale length of the disk.

In our work we use a system of galactic units where  $G = 1$ , the unit of length is 1 kpc and the unit of velocity is  $10 \text{ km s}^{-1}$ . Thus, the unit of time is  $0.9778 \times 10^8 \text{ yr}$ , the unit of mass is  $2.325 \times 10^7 M_\odot$ , the unit of angular momentum (per unit mass) is  $10 \text{ km kpc s}^{-1}$ , and the unit of energy (per unit mass) is  $100 \text{ km}^2 \text{ s}^{-2}$ . In these units, the values of the involved parameters are:  $M_n = 500$  (corresponding to  $1.162 \times 10^{10} M_\odot$ ),  $c_n = 0.25$ ,  $M_d = 7000$  (corresponding to  $1.627 \times 10^{11} M_\odot$ ),  $\alpha = 3$ , and  $h = 0.175$ . The values of the nucleus and the disk were chosen with a Milky Way-type galaxy in mind (e.g., Allen & Santillán 1991). Furthermore, the above-mentioned values of the parameters are kept constant throughout the numerical calculations and define the Standard Model (S.M.) which secures everywhere a positive mass density and is free of singularities.

Due to the fact that the disk galaxy is axially symmetric, the  $z$  component of the total angular momentum is conserved. Exploiting this property we can describe orbits by means of the effective potential

$$\Phi_{\text{eff}}(R, z) = \Phi(R, z) + \frac{L_z^2}{2R^2}. \quad (3)$$

The value of the angular momentum of all orbits is  $L_z = 10$  and remains constant throughout.

In this case, the set of equations of motion in the meridional plane is

$$\ddot{R} = -\frac{\partial \Phi_{\text{eff}}}{\partial R}, \quad \ddot{z} = -\frac{\partial \Phi_{\text{eff}}}{\partial z}, \quad (4)$$

while the variational equations needed for the calculation of chaos indicators (in this case the SALI, see §3) are

$$\begin{aligned} (\delta \dot{R}) &= \delta \dot{R}, \quad (\delta \dot{z}) = \delta \dot{z}, \\ (\delta \ddot{R}) &= -\frac{\partial^2 \Phi_{\text{eff}}}{\partial R^2} \delta R - \frac{\partial^2 \Phi_{\text{eff}}}{\partial R \partial z} \delta z, \\ (\delta \ddot{z}) &= -\frac{\partial^2 \Phi_{\text{eff}}}{\partial z \partial R} \delta R - \frac{\partial^2 \Phi_{\text{eff}}}{\partial z^2} \delta z. \end{aligned} \quad (5)$$

The corresponding Hamiltonian to the effective potential (3) reads

$$H(R, z, \dot{R}, \dot{z}) = \frac{1}{2} (\dot{R}^2 + \dot{z}^2) + \Phi_{\text{eff}}(R, z) = E, \quad (6)$$

where  $\dot{R}$  and  $\dot{z}$  are momenta per unit mass, conjugate to coordinates  $R$  and  $z$ , respectively, while  $E$  is the numerical value of the Hamiltonian, which is conserved.

Consequently, a trajectory is restricted to the area in the  $(R, z)$  plane, satisfying  $E \geq \Phi_{\text{eff}}(R, z)$ , while all the other regions are forbidden to the star motion.

### 3. COMPUTATIONAL METHODS

For the investigation of the orbital dynamics (regularity or chaoticity) of the galaxy model, we need to establish some sets of initial conditions of orbits. For this purpose we define, for several values of energy  $E$ , dense uniform grids of  $1024 \times 1024$  initial conditions in the phase space  $(R, \dot{R})$  regularly distributed in the area allowed by the value of the Hamiltonian  $E$ . The initial conditions of the orbits whose properties will be examined are defined as follows: we consider orbits with the initial conditions  $(R_0, \dot{R}_0)$  with  $z_0 = 0$ , while the value of  $\dot{z}_0$  is always obtained from the Hamiltonian (6). For each initial condition a double precision Bulirsch-Stoer FORTRAN 77 algorithm (e.g., Press et al. 1992) is used for the numerical integration of the equations of motion (4) as well as the variational equations (5). The time step of the numerical integration is  $10^{-2}$  and our tests suggest that the results do not change by halving the time step. In all calculations the Hamiltonian (Eq. 6) was conserved better than one part in  $10^{-11}$ , although for the majority of the initial conditions it was better than one part in  $10^{-12}$ .

The phase space is divided into the ordered and chaotic space. Over the years, several chaos indicators have been developed in order to determine the character of orbits. In our case, we chose to use the Smaller ALignment Index (SALI) method. The SALI (Skokos 2001) has proved a very fast, reliable and effective tool, which is defined as

$$\text{SALI}(t) \equiv \min(d_-, d_+), \quad (7)$$

where  $d_- \equiv \|\mathbf{w}_1(t) - \mathbf{w}_2(t)\|$  and  $d_+ \equiv \|\mathbf{w}_1(t) + \mathbf{w}_2(t)\|$  are the alignments indices, while  $\mathbf{w}_1(t)$  and  $\mathbf{w}_2(t)$  are two deviation vectors which initially point in two random directions. For distinguishing between ordered and chaotic motion, all we have to do is to compute the SALI along time interval  $t_{\text{max}}$  of numerical integration. In particular, we track simultaneously the time-evolution of the main orbit itself as well as the two deviation vectors  $\mathbf{w}_1(t)$  and  $\mathbf{w}_2(t)$  in order to compute the SALI. The time-evolution of SALI strongly depends on the nature of the computed orbit: in the case of a regular orbit, the SALI exhibits small fluctuations around non-zero values, but when the orbit is chaotic, after a small transient period the SALI tends exponentially to zero, approaching the limit of the accuracy of the computer ( $10^{-16}$ ). Therefore, the particular time-evolution of the SALI allows us to distinguish fast and safely between regular and chaotic motion. Nevertheless, we have to define a specific numerical threshold value for determining the transition from order to chaos. After conducting extensive numerical experiments, integrating many sets of orbits, we conclude that a safe threshold value for the SALI is  $10^{-8}$ . In order to decide whether the orbit is regular or chaotic, one may follow the usual method according to which we check, after a certain and predefined time interval of numerical integration, if the value of SALI becomes less than the established threshold value. Therefore, if  $\text{SALI} \leq 10^{-8}$ , the orbit is chaotic, while when  $\text{SALI} > 10^{-8}$  the orbit is regular, thus making the distinction between regular and chaotic motion clear and beyond any doubt. For the computation of SALI we used the LP-VI code (Carpintero et al. 2014), a fully operational routine which efficiently computes a suite of many chaos indicators for dynamical systems

in any number of dimensions.

The total integration time is an element of paramount importance. In our case, each initial condition is integrated for  $10^4$  time units ( $10^{12}$  yr) which correspond to a time span of the order of hundreds of orbital periods. We have chosen to apply such a large time interval having in mind the occasion of “sticky” orbits<sup>1</sup>. Here it should be emphasized that a sticky orbit could be easily misclassified as ordered by any chaos indicator if the integration period is too low, so that the orbit does not have enough time to unveil its chaotic character. Setting the integration interval to  $10^4$  we manage to correctly classify orbits with sticky periods of at least 100 Hubble times. Orbits with higher sticky periods do not have any physical meaning and are completely out of the scope of the present work.

Before closing this section, we should better clarify an issue regarding the nomenclature of the orbits. It is well known that in axisymmetric potentials all orbits are in fact three-dimensional loop orbits that always circulate in the same direction around the  $z$ -axis of symmetry. In the meridional plane, however, the meaning of the rotation is lost and therefore the path that an orbit follows onto the  $(R, z)$  plane can take any shape. In this work, as in all previous related papers, we characterize an orbit by taking into account its motion in the meridional plane. For instance, if the orbit is a rosette in the 3D system, it will be a linear orbit in the  $(R, z)$  plane, a closed tube orbit will be a meridional 2:1 banana-type orbit, etc. Furthermore, it should be emphasized that the term “box” orbit is used for the orbit that conserves circulation but this refers **only** to the circulation provided by the meridional plane itself. These orbits were originally characterized as “boxes” (e.g., Ollongren 1962) due to their boxlike shape, even though their shapes in three-dimensions are more similar to doughnuts (see the review of Merritt 1999). In order to maintain the continuity with all previous related works we decided to keep this initial formalism.

#### 4. ORBIT CLASSIFICATION

In this section we will investigate the orbital content of the galaxy for several energy levels. We use the sets of initial conditions of orbits analyzed in Section 3 in order to construct the respective grids in the phase plane. It should be emphasized that the energy level controls the actual size of the grid and particularly the  $R_{\max}$  which is the maximum possible value of the  $R$  coordinate. We choose the values of the energy which yield  $3 \text{ kpc} < R_{\max} < 18 \text{ kpc}$ . Once the value of the energy is chosen and the corresponding grid is determined, we integrate the initial conditions of orbits, calculate the SALI and then classify ordered orbits into regular families.

Our numerical calculations suggest that in our axially symmetric galaxy model there are eight basic types of orbits: (i) chaotic orbits; (ii) box orbits; (iii) 1:1 linear orbits; (iv) 2:1 banana-type orbits; (v) 2:3 fish-type orbits; (vi) 4:3 resonant orbits; (vii) 6:5 resonant orbits and (viii) orbits with other secondary resonances (i.e., all resonant orbits not included in the former categories). It turns out that for each resonant family included in the “other” category the corresponding percentage is less than 1% in all examined cases, and therefore their contribution to the overall

---

<sup>1</sup> Usually a “sticky” orbit behaves regularly for long time periods before it finally drifts away from the boundaries of ordered regions and starts to wander in the chaotic domain, thus fully revealing its true chaotic nature.

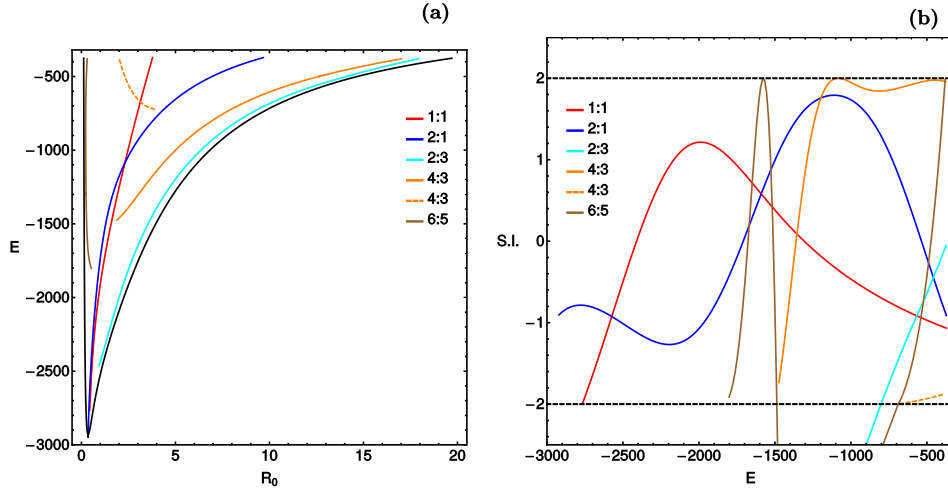


**Fig. 1.** Panel (a): the  $(R_0, E)$  characteristic curves of all the orbital families. Panel (b): the evolution of the stability index (S.I.) of all the families of periodic orbits shown in panel (a) as a function of the orbital energy  $E$ . The black horizontal dashed lines at  $-2$  and  $+2$  delimit the range of S.I. for which the periodic orbits are stable.

orbital structure of the galaxy is practically insignificant. The  $n : m$  notation<sup>2</sup> we use for the regular orbits is according to Carpintero & Aguilar (1998) and Zotos & Carpintero (2013), where the ratio of these integers corresponds to the ratio of the main frequencies of the orbit, where main frequency is the frequency of the greatest amplitude in each coordinate. Main amplitudes, when having a rational ratio, define the resonances of an orbit. The shapes of all of the basic types of orbits are shown in Fig. 3 of Paper I.

Panel (a) of Fig. 1 presents the so-called “characteristic” diagram which shows the evolution of the initial condition  $R_0$  of the parent periodic orbits of each resonant family as a function of the total orbital energy  $E$ . Here we would like to point out that for orbits launched perpendicular to the  $R$ -axis only the initial condition  $R_0$  is needed to locate them on this informative diagram. For orbits not starting perpendicularly to the  $R$ -axis (i.e., the 1:1 family), we need pairs of initial position-velocity  $(R_0, \dot{R}_0)$  and, therefore, the characteristic diagram is now three-dimensional. In the two-dimensional characteristic diagrams of panel (a) we observe that the curve of the 1:1 resonant family crosses two other characteristic curves. Here it should be clarified that the full characteristic curve of the 1:1 resonant family is three-dimensional since  $\dot{R}_0 \neq 0$ , however we decided to combine all families together in a two-dimensional plot containing only the evolution of the  $R$  coordinate (of course, in the 3D  $(R, \dot{R}, E)$  space the corresponding characteristic curves do not cross one another). The outermost black solid line denotes the permissible area of motion inside the potential well  $\Phi_{\text{eff}}(R, z = 0)$ . In Fig. 1b, we present the so-called “stability” diagram which indicates the stability of all of the resonant families as the numerical value of the energy varies. This plot gives us the ability to examine the evolution of the stability index (S.I.) (Meyer & Hall

<sup>2</sup> An  $n : m$  resonant orbit would be represented by  $m$  distinct islands of invariant curves in the  $(R, \dot{R})$  phase plane and  $n$  distinct islands of invariant curves in the  $(z, \dot{z})$  surface of section.

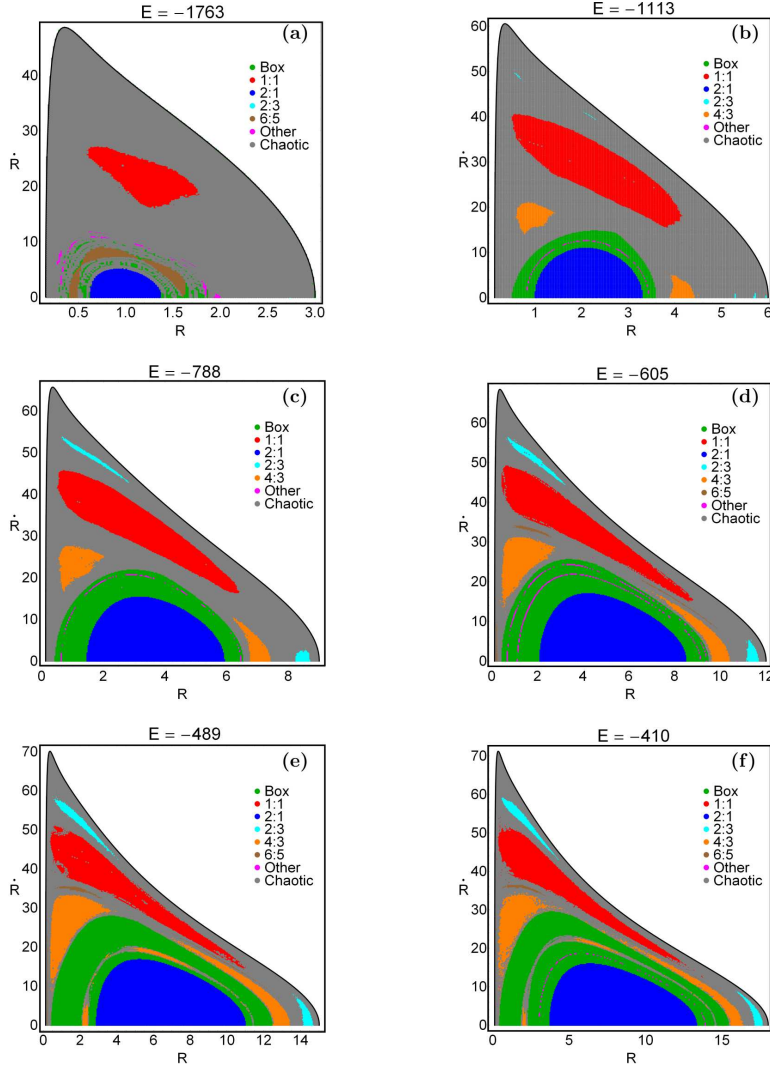
1992; Zotos 2013) of the resonant periodic orbits as a function of energy and also to monitor all the transitions from instability to stability and vice versa. We shall recall that a periodic orbit is stable if S.I. is between  $-2$  and  $+2$ . Our calculations reveal that the 2:1 resonant family is stable throughout the energy range ( $E \in [-2946, -310]$ ). The 1:1 resonant family starts at  $E = -2764.88$  and remains stable throughout. Moreover, the 2:3 resonant family begins at  $E = -2462.07$  and is unstable in the interval  $-2462.07 \leq E \leq -804.71$ . Similarly, the starting point of the 4:3 resonant family is at  $E = -1474.07$ . Looking carefully at panels (a) and (b) we see that there is a second smaller and stable branch of the 4:3 resonant family (shown as a dashed line) for  $-722.12 \leq E \leq -371$ . Finally, the 6:5 resonant family initiates at  $E = -1802.01$  and is unstable only in the interval  $-1359.24 \leq E \leq -686.91$ .

Fig. 2 with panels from (a) to (f) presents six grids of initial conditions ( $R_0, \dot{R}_0$ ) of orbits that we have classified for different values of the orbital energy. These color-coded grids are equivalent to the classical Poincaré Surface of Section (PSS) and help us to determine what types (families) of orbits occupy specific domains in the phase plane ( $R, \dot{R}$ ). The outermost thick black curve is the limiting curve in the phase space which is defined as

$$\frac{1}{2}\dot{R}^2 + \Phi_{\text{eff}}(R, z=0) = E. \quad (8)$$

Panel (a) of Fig. 2 shows the grid for a very low energy level. This level corresponds to local motion around the dense and massive nucleus. Therefore, we observe that the vast portion of the plane is covered by initial conditions of chaotic orbits. There are two main stability domains corresponding mainly to 2:1 and 1:1 resonant orbits. Around the 2:1 stability island we identify delocalized initial conditions of box orbits and a chain of 6:5 stability islands. In addition, above the 6:5 stability islands we observe the presence of scattered initial conditions corresponding to higher order resonant orbits (mainly 6:7 and 8:7 resonant orbits). In Fig. 2b the energy level is  $E = -1113$ . Here, several differences with respect to the previous grid are observable: (i) the amount of chaos has decreased, while the stability islands of 2:1 and 1:1 resonant orbits occupy a greater area in the phase plane; (ii) the initial conditions of box orbits form an open ring above the 2:1 stability island; (iii) the stability islands of the 4:3 resonance have emerged; (iv) some initial conditions corresponding to 2:3 resonant orbits are identified inside the unified chaotic sea. The stability diagram shown in Fig. 1b indicates that the 2:3 resonance is unstable for  $E = -1113$ , therefore it is impossible to form well-defined stability islands like the other resonances. Inside the box region there is a stripe of initial conditions that correspond to the 7:5 resonance. As the energy increases, the extent of the chaotic domain decreases. This is clear in Fig. 2c where  $E = -788$ . In this case, the 2:3 resonance is stable and therefore we can see the two<sup>3</sup> corresponding stability islands. We should also mention that the 6:5 resonance is absent in the grids of Figs. 2b and 2c. This, however, is anticipated because the 6:5 resonance is unstable for  $-1359.24 \leq E \leq -686.91$  (see Fig. 1b) and therefore the corresponding periodic point is deeply buried in the chaotic sea.

<sup>3</sup> It must be emphasized that the color-coded grids shown in Fig. 2(a-f) present only the  $\dot{R} > 0$  part of the phase plane ( $R, \dot{R}$ ); the  $\dot{R} < 0$  part is symmetrical. Therefore, in many resonant cases not all of the corresponding stability islands are shown (e.g., for the 2:3 and 4:3 resonances only two (one and a half to be more precise) of the total three islands are present).



**Fig. 2.** Orbital structure of the phase plane  $(R, \dot{R})$  of our disk galaxy model for different values of the total orbital energy  $E$ .

Fig. 2d is quite similar to Fig. 2c, with only minor differences. The 6:5 resonance emerges again, while in the box area there are two small filaments of initial conditions corresponding to secondary resonances (5:4 and 7:5). When  $E = -489$ , we observe in Fig. 2e that the chaotic sea is reduced to a chaotic layer situated at the outer parts of the phase plane. We also see the presence of the second chain of the 4:3 resonance inside the box region, while secondary and higher resonant orbits seem to be absent in this case. It should be pointed out that our result for  $E = -489$  is quite similar to that presented in Fig. 18a of Paper I (the only differences are due to improvements in the classification code). Finally, in Fig. 2f we present the orbital structure of the phase plane for  $E = -410$ . It is seen that



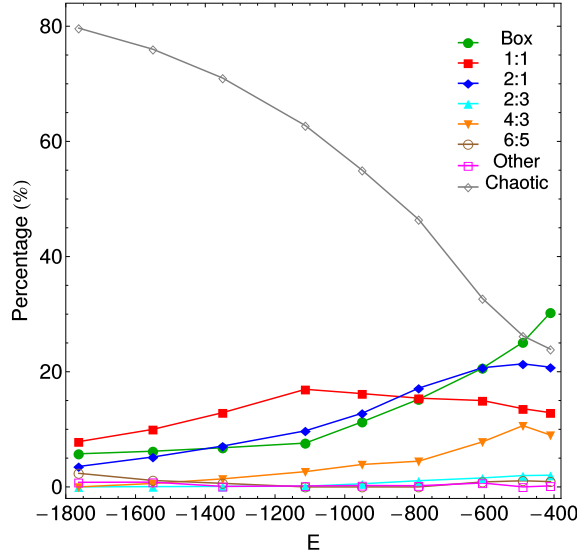


**Fig. 3.** Evolution of the percentages of different types of orbits in the phase plane  $(R, \dot{R})$  of our galaxy model as a function of the total orbital energy  $E$ .

the structure is very similar to that Fig. 2e discussed above. Inside the box region one can identify tiny chains of initial conditions corresponding to either 5:4 or 9:7 resonance. For relatively high energy levels, or, in other words, for global motion of stars, we see that the orbital content remains almost the same regardless of the orbital energy shift.

The evolution of the percentages of all types of orbits as a function of the total orbital energy  $E$  is shown in Fig. 3. We observe that for low energy levels, corresponding to local motion around the central nucleus, chaotic motion dominates which covers about 80% of the entire phase plane. As we proceed to higher energy levels however, the percentage of chaos decreases constantly and, at the highest energy level studied, chaos occupies only about 10% of the phase space. On the other hand, the rate of many regular families grows with increasing energy. In particular, the percentage of box orbits exhibits an almost exponential increase and for  $E = -410$  it is the most populated family, implying that in global motion the majority of the stars perform box orbits. The percentage of 2:1 resonant orbits also increases, however for  $E > -600$  it seems to saturate around 20%. Furthermore, the percentages of 1:1 and 4:3 resonant orbits initially grow, but they drop for  $E > -1100$  and  $E > -500$ , respectively. Moreover, we could say that, in general terms, all the other resonant families (2:3, 6:5 and other) possess throughout very low percentages (always less than 3%), thus varying the value of the energy only shuffles the orbital content among them. Therefore, taking into account all the above-mentioned numerical analysis, we may conclude that in the phase space  $(R, \dot{R})$  the types of orbits that are mostly influenced by the value of the orbital energy are box, 1:1, 2:1, 4:3 and chaotic orbits. In general terms, the numerical

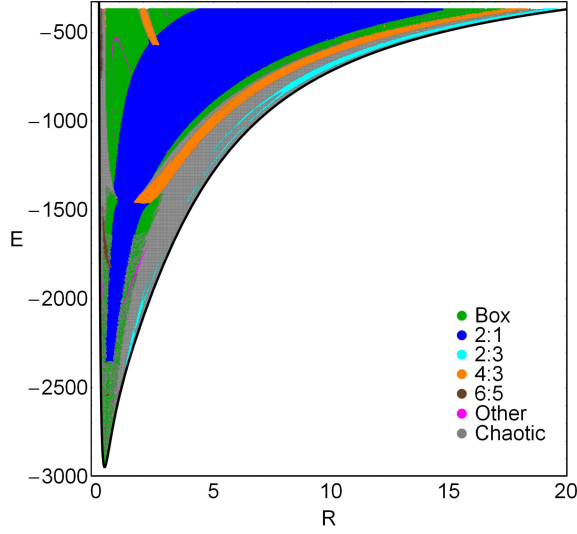


**Fig. 4.** Orbital structure of the  $(R, E)$  plane showing a detailed analysis of the evolution of orbits starting perpendicularly to the  $R$ -axis when the value of energy varies in the interval  $E \in [-2946, -371]$ .

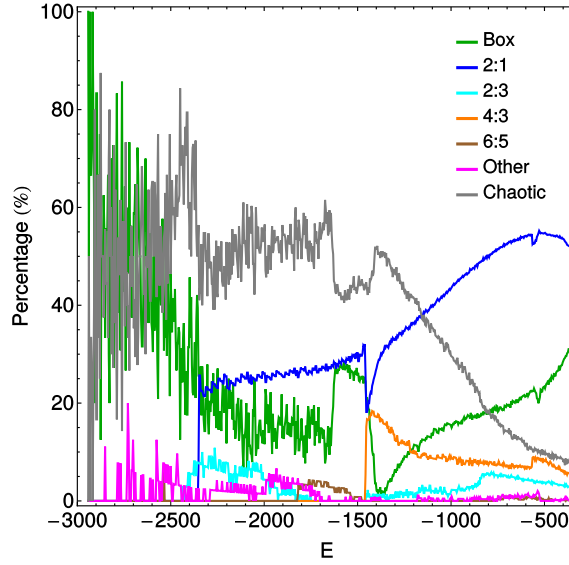


**Fig. 5.** Evolution of the percentages of different types of orbits in the  $(R, E)$  plane of our galaxy model as a function of the total orbital energy  $E$ .

outcomes presented in Fig. 3 coincide with those reported in Fig. 18b of Paper I.

## 5. AN OVERVIEW ANALYSIS

The color-coded grids in the phase space  $(R, \dot{R})$  presented in Figs. 2a–2f can provide information on the phase space mixing, but only for a fixed value of the energy integral. Back in the late 60s Hénon conceived a new type of plane using the section  $z = \dot{R} = 0$ ,  $\dot{z} > 0$ . In this case, all the stars are launched from the horizontal  $R$  axis, parallel to the vertical  $z$  axis and in the positive direction. This plane provides also information regarding areas of regularity and chaotic domains, but, in contrast to the previously described type of grids, only orbits with pericenters on the horizontal axis are included. Therefore, the value of the Hamiltonian  $E$  can be used as an ordinate giving us the ability to investigate a continuous spectrum of energy values rather than a few discrete energy levels. In Fig. 4 we present the orbital structure of the  $(R, E)$  plane when  $E \in [-2946, -371]$ . We clearly distinguish several stability regions of resonant islands and chaotic layers. Once more, in order to explore with sufficient accuracy the evolution of the types of orbits, we defined dense uniform grids of  $1024 \times 1024$  initial conditions in the  $(R, E)$  space. The plot shown in Fig. 4 reminds us a lot of the characteristic diagram presented earlier in Fig. 1a. At high energy levels, we observe that inside the box region, several families of other higher resonances are present producing thin filaments of initial conditions.

In addition, in Fig. 5 we provide a diagram showing the evolution of the percentages of all types of orbits as a function of the energy. This diagram is quite similar to that presented in Fig. 3 but in this case each curve is composed of a continuous spectrum of the values of energy. Here it should be pointed out that the  $(R, E)$  plane contains only such orbits which start perpendicularly to the  $R$  axis. Therefore, the 1:1 resonant family for which the initial conditions are pairs of position-velocity is obviously not included. It is evident that, for very low values of energy ( $E < -2500$ ), the  $(R, E)$  plane is dominated mainly by a mixture of box and chaotic orbits. For intermediate energy levels ( $-2500 < E < -1500$ ), we see that the percentages of all types of orbits exhibit minor fluctuations, thus remaining almost constant. For higher energy levels ( $E > -1500$ ), however, we observe that the increase on the energy influences, more or less, the populations of all types of orbits. In particular, the percentage of chaotic orbits decreases from about 50% to about 10%, while at the same time the rates of box and 2:1 resonant orbits grow almost linearly and at the highest energy level studied ( $E = -371$ ) they occupy about 30% and 55% of the  $(R, E)$  plane, respectively. Furthermore, the percentages of the 2:3 and 4:3 resonant families seem to saturate around 5%, while the rates of the 6:5 family and other types of orbits remain very low (around 1%).

## 6. DISCUSSION AND CONCLUSIONS

In this work we adopted the analytic axisymmetric galactic gravitational potential introduced in Paper I and attempted to explore how the value of the total orbital energy influences the level of chaos and also the distribution of the main regular families. Our numerical investigation took place in the meridional  $(R, z)$  plane, in order to reduce the three dimensional motion into two dimensions. Moreover, the values of all the other dynamical quantities entering the system were kept constant throughout so as to monitor the evolution of the percentages of all types of orbits as a function of the energy. Our detailed and systematic numerical investigation revealed that the populations of the regular families as well as the amount

of chaos are indeed very dependent on the value of the energy.

For a better understanding of the orbital properties of the galactic system we examined the structure of the phase space  $(R, \dot{R})$ . For distinguishing between order and chaos we defined dense grids of  $1024 \times 1024$  initial conditions of orbits uniformly distributed within the area defined by the corresponding energy level. Then, for illustrating how the energy influences the orbital structure, we presented in each case color-coded grids, thus visualizing what types of orbits occupy specific domains of the phase space. Each initial condition was numerically integrated for a time period of  $10^4$  time units which corresponds to  $10^{12}$  yr. Our choice regarding the integration time allowed us to eliminate sticky orbits with periods of at least 100 Hubble times. Initially our numerical code used the SALI method to identify the regular or chaotic nature of the orbits and then a frequency analysis technique was applied in order to classify regular orbits into different families.

The most important results of our numerical investigation can be summarized as follows:

- The SALI has been proved, once more, a very reliable dynamical indicator which allowed us to safely distinguish between regular and chaotic initial conditions of orbits relatively fast and with great accuracy.
- In the phase space of our composite gravitational model, several regular types of orbits were found to exist, while strong and extended chaotic areas separating the stability domains were also present. In particular, a wide plethora of resonant orbits (i.e., 1:1, 2:1, 2:3, 4:3, 6:5 and other higher resonant orbits) have been identified thus making the orbital content of the system more rich.
- We revealed that in the phase space  $(R, \dot{R})$  the box, 1:1, 2:1, 4:3 and chaotic orbits are those mainly influenced by the change in the value of the energy. Furthermore, it was observed that most of the resonant families are stable, although they were found in specific energy ranges in which some resonant families (i.e., the 2:3 and 6:5) become unstable.
- We examined the orbital content of several isolated energy levels. It was found that for low energy levels that correspond to local motion around the dense and massive spherical nucleus the motion of stars is highly chaotic, but as the value of the energy increases, leading to global motion, the amount of the observed chaos gradually decreases and regular motions take over the phase space.
- We proceeded one step further constructing the  $(R, E)$  plane so as to monitor the evolution of all types of orbits as a function of the energy. It is found that at very low energies there is a strong mixture of box and chaotic orbits which, however, dissolves as the energy increases, thus giving room to many other types of regular resonant orbits to grow.

Judging by the detailed outcomes we may say that our task has been successfully completed. We hope that the present analysis and the corresponding numerical results will be useful in the field of orbit classification in galaxy models. Taking into account that our results are encouraging, it is in our future plans to properly modify our dynamical model in order to expand our investigation into

three dimensions and explore the entire six-dimensional phase space thus revealing the influence of the value of the energy on the orbital structure.

ACKNOWLEDGMENTS. We would like to express our warmest thanks to Dr. Leonid P. Ossipkov (University of Petersburg) for the careful reading of the manuscript and for all suggestions and comments which allowed us to improve both the quality and the clarity of our paper.

#### REFERENCES

- Allen C., Santillán A. 1991, RMxAA, 22, 255  
 Binney J., Spergel D. 1982, ApJ, 252, 308  
 Binney J., Spergel D. 1984, MNRAS, 206, 159  
 Binney J., Tremaine S. 2008, *Galactic Dynamics*, 2nd ed., Princeton Univ. Press  
 Caranicas N. D., Zotos E. E. 2013, PASA, 30, 49  
 Carpintero D. D., Aguilar L. A. 1998, MNRAS, 298, 1  
 Carpintero D. D., Maffione N., Darriba L. 2014, Astronomy and Computing, 5, 19  
 Hasan H., Norman C. A. 1990, ApJ, 361, 69  
 Hasan H., Pfenniger D., Norman C. 1993, ApJ, 409, 91  
 Laskar J. 1988, A&A, 198, 341  
 Laskar J. 1993, Physica D, 67, 257  
 Merritt D. 1999, PASP, 111, 129  
 Meyer K. R., Hall G. R. 1992, *Introduction to Hamiltonian Dynamical Systems and the N-Body Problem*, Springer-Verlag  
 Miyamoto W., Nagai R. 1975, PASJ, 27, 533  
 Ollongren A. 1962, Bull. Astron. Inst. Netherlands, 16, 241  
 Press H. P., Teukolsky S. A., Vetterling W. T., Flannery B. P. 1992, *Numerical Recipes in FORTRAN 77*, 2nd Ed., Cambridge Univ. Press  
 Šidlichovský M., Nesvorný D. 1996, CeMDA, 65, 137  
 Skokos C. 2001, J. Phys. Math. Gen., 34, 10029  
 Zotos E. E. 2012, New Astronomy, 17, 576  
 Zotos E. E. 2013, Nonlinear Dynamics, 73, 931  
 Zotos E. E. 2014a, A&A, 563, A19  
 Zotos E. E. 2014b, Baltic Astronomy, 23, 37  
 Zotos E. E. 2014c, Mechanics Research Communications, 62, 102  
 Zotos E. E. 2014d, Baltic Astronomy, 23, 151  
 Zotos E. E., Caranicas N. D. 2013, A&A, 560, A110  
 Zotos E. E., Caranicas N. D. 2014, Nonlinear Dynamics, 76, 323  
 Zotos E. E., Carpintero D. D. 2013, CeMDA, 116, 417 (Paper I)